

## Article

# Photoreactive Carbon Dots Modified g-C<sub>3</sub>N<sub>4</sub> for Effective Photooxidation of Bisphenol-A under Visible Light Irradiation

Anwar Iqbal <sup>1</sup>, Fatimah Bukola Shittu <sup>1</sup>, Mohamad Nasir Mohamad Ibrahim <sup>1</sup>, N. H. H. Abu Bakar <sup>1</sup>,  
Noorfatimah Yahaya <sup>2</sup>, Kalaivizhi Rajappan <sup>3</sup>, M. Hazwan Hussin <sup>1</sup>, Wan Hazman Danial <sup>4</sup>  
and Lee D. Wilson <sup>5,\*</sup>

<sup>1</sup> School of Chemical Sciences, Universiti Sains Malaysia, Gelugor, Penang 11800, Malaysia

<sup>2</sup> Integrative Medicine Cluster, Advanced Medical and Dental Institute, Universiti Sains Malaysia, Bertam, Kepala Batas, Penang 13200, Malaysia

<sup>3</sup> Department of Chemistry, SRM Institute of Science and Technology, Kattankulathur, Chengalpattu 603203, India

<sup>4</sup> Department of Chemistry, Kulliyah of Science, International Islamic University Malaysia, Kuantan 25200, Malaysia

<sup>5</sup> Department of Chemistry, University of Saskatchewan, 110 Science Place, Room 165 Thorvaldson Building, Saskatoon, SK S7N 5C9, Canada

\* Correspondence: lee.wilson@usask.ca; Tel.: +1-306-966-2961



**Citation:** Iqbal, A.; Shittu, F.B.; Ibrahim, M.N.M.; Bakar, N.H.H.A.; Yahaya, N.; Rajappan, K.; Hussin, M.H.; Danial, W.H.; Wilson, L.D. Photoreactive Carbon Dots Modified g-C<sub>3</sub>N<sub>4</sub> for Effective Photooxidation of Bisphenol-A under Visible Light Irradiation. *Catalysts* **2022**, *12*, 1311. <https://doi.org/10.3390/catal12111311>

Academic Editors: Detlef W. Bahnemann, Ewa Kowalska, Ioannis Konstantinou, Magdalena Janus, Vincenzo Vaiano, Wonyong Choi and Zhi Jiang

Received: 27 September 2022

Accepted: 21 October 2022

Published: 25 October 2022

**Publisher's Note:** MDPI stays neutral with regard to jurisdictional claims in published maps and institutional affiliations.



**Copyright:** © 2022 by the authors. Licensee MDPI, Basel, Switzerland. This article is an open access article distributed under the terms and conditions of the Creative Commons Attribution (CC BY) license (<https://creativecommons.org/licenses/by/4.0/>).

**Abstract:** A series of carbon dots (CDs) modified g-C<sub>3</sub>N<sub>4</sub> (xCDs/g-C<sub>3</sub>N<sub>4</sub>; x = 0.5, 1.0, and 1.5 mL CDs solution) was synthesized via the microwave-assisted hydrothermal synthesis method for the photooxidation of bisphenol-A (BPA) under visible light irradiation. The X-ray diffraction (XRD) analysis indicates that the CDs may have a turbostratic structure and the resulting photocatalysts have distorted crystal structure, as compared with pure g-C<sub>3</sub>N<sub>4</sub>. The high-resolution transmission electron microscope (HR-TEM) analysis revealed amorphous, mono-disperse, spherical CDs with an average particle size of 3.75 nm. The distribution of CDs within the matrix of g-C<sub>3</sub>N<sub>4</sub> appear as small dark dot-like domains. The N<sub>2</sub> adsorption-desorption analysis indicates that the nanocomposites are mesoporous with a density functional theory (DFT) estimate of the pore size distribution between 2–13 nm. The CDs quantum yield (QY) was determined to be 12% using the UV-vis spectral analysis, where the CDs/g-C<sub>3</sub>N<sub>4</sub> has improved absorption in the visible region than g-C<sub>3</sub>N<sub>4</sub>. The higher BET surface area of CDs/g-C<sub>3</sub>N<sub>4</sub> provided more adsorption sites and the ability to yield photogenerated e<sup>-</sup>/h<sup>+</sup> pairs, which caused the 1.5 CDs/g-C<sub>3</sub>N<sub>4</sub> to have better photocatalytic efficiency compared to the rest of the systems. The highest removal, 90%, was achieved at the following optimum conditions: BPA initial concentration = 20 mg L<sup>-1</sup>, catalyst dosage = 30 mg L<sup>-1</sup>, and pH = 10. The photooxidation process is mainly driven by photogenerated holes (h<sup>+</sup>) followed by •OH and O<sub>2</sub>•<sup>-</sup>. The synthesis of the 1.5 CDs/g-C<sub>3</sub>N<sub>4</sub> system is simple and cost-effective, where this photocatalyst is highly stable and reusable versus other systems reported in the literature.

**Keywords:** carbon quantum dots; g-C<sub>3</sub>N<sub>4</sub>; bisphenol-A; photocatalysis; visible light irradiation

## 1. Introduction

Theo Colborn and colleagues introduced the term “endocrine disruptor” in the 1990s. The group later issued an agreement about the effects of Endocrine Disrupting Chemicals (EDCs) on human and environmental health known as the Wingspread Statement [1]. The Endocrine Society defines endocrine disruptors (EDs) as “an exogenous chemical, or a mixture of chemicals, that can interfere with any aspect of hormone action” [2]. They include pharmaceuticals, dioxin, and dioxin-like compounds, polychlorinated biphenyls, organochlorinated pesticides, and plasticizers [3–5]. EDs can interfere with hormonal functions and are considered a threat to humans and animals. Bisphenol A (BPA) is a synthetic estrogen that is widely used in the production of toys, baby bottles, drinking

bottles, food containers, water pipes and medical devices [6]. BPA has been classified among EDs by the US Environmental Protection Agency (EPA) and the World Wide Fund (WWF) for Nature [7]. Even at low concentrations, BPA can induce estrogenic effects, which contributes to reproductive and developmental disorders [8].

BPA can be found in water columns since it enters aquatic systems as effluent from sewage treatment plants or factories, landfill leachate, and degradation by-products of plastic litter [9]. Wastewater treatment methods such as chlorination, filtration, sedimentation, ozonation, and ultraviolet irradiation face technological difficulties, including secondary contamination, recolonization, and high energy usage [10], whereas conventional water treatment techniques are unable to remove EDs effectively [11]. Photocatalysis is a technique that utilizes semiconductors and light irradiation to generate reactive oxygen species (ROS), such as superoxide ( $O_2^{\bullet-}$ ) and hydroxyl radicals ( $OH^\bullet$ ). These ROS are powerful and able to mineralize organic pollutants, including BPA. For the photocatalytic process to effectively take place, the semiconductors must be able to utilize light irradiation effectively and with stability, along with the ability to suppress the recombination rate of photogenerated electron/hole ( $e^-/h^+$ ) pairs and transport them efficiently.

Graphitic carbon nitride ( $g-C_3N_4$ ) is an allotrope of all carbon nitride that is relatively easy to synthesize and low cost, which has high chemical stability, low density, favourable visible-light photocatalytic behaviour, short band-gap energy (2.65 eV), and good biocompatibility [12]. These features enable  $g-C_3N_4$  to be developed into a photocatalyst comparable to  $TiO_2$  and  $ZnO$ . However, due to incomplete polymerization, the presence of unreacted amino groups in pure  $g-C_3N_4$  can decrease its photocatalytic ability. The unreacted amino groups are structural defects that act as a recombination center for photogenerated electron-hole ( $e^-/h^+$ ) pairs during photocatalytic reactions that reduce charge efficiency [13]. The high recombination rate of the  $e^-/h^+$  pairs reduce the amount of ROS generated for effective photodegradation.

As a new and environmentally friendly carbon-based nanomaterial class, carbon dots (CDs) or carbon quantum dots (CQDs) have been widely used recently in catalysis due to their low toxicity, ease of synthesis, and high chemical stability [14]. They are zero-dimensional structures of less than 10 nm with  $sp^2$  conjugated cores [15]. CDs have excellent electron transfer ability, which upon combination with another semiconductor, suppresses the recombination of photogenerated  $e^-/h^+$  pairs, and increases the absorption range to the visible light region. This design is anticipated to improve the photocatalytic performance [16] (cf. Table 1). Accordingly,  $g-C_3N_4$  modified with CQDs are versatile and can be used as an effective photocatalyst in the photooxidation of various organic pollutants under UV and visible light irradiation. Based on the examples provided in Table 1, the CDs or CQDs enhance the photocatalytic activity of  $g-C_3N_4$  by preventing rapid recombination of  $e^-/h^+$  pairs, enhancing the absorption of visible light, including enhancement of the photoluminescence (PL) properties of the photocatalysts.

Regardless, the potential of  $g-C_3N_4$  modified CDs in the photodegradation of BPA under visible light intensity was rarely discussed in terms of the kinetics and mechanism of the process to the best of our knowledge. Herein, a high-efficiency  $g-C_3N_4$  modified CDs ( $CDs/g-C_3N_4$ ) photocatalyst was prepared by a facile microwave synthesis, followed by thermal polymerization for the photooxidation of BPA under visible light irradiation. The  $CDs/g-C_3N_4$  demonstrated good photocatalytic potential compared to pristine  $g-C_3N_4$  and other photocatalysts reported in the literature. The structure-activity relationship was explored in detail. Based on the collected data, a potential charge transfer mechanism, kinetics, and photocatalytic transformation for BPA degradation was proposed herein.

**Table 1.** Graphitic carbon nitride (g-C<sub>3</sub>N<sub>4</sub>) modified carbon quantum dots for various organic pollutants.

Photocatalyst	Application	Outcome and Role of CDs/CQDs	Ref
C-dots/g-C <sub>3</sub> N <sub>4</sub>	Photodegradation of Rhodamine B (RhB) dye under UV light irradiation.	<ul style="list-style-type: none"> <li>The C-dots/ g-C<sub>3</sub>N<sub>4</sub> have higher activity kinetic constant (~4 min<sup>-1</sup>), compared to g-C<sub>3</sub>N<sub>4</sub> (~1.75 min<sup>-1</sup>).</li> <li>The C-dots increased the g-C<sub>3</sub>N<sub>4</sub>, interlayer layer distance, and surface area.</li> </ul>	[17]
Zero-dimensional carbon quantum dots (CQDs) immobilized within one-dimensional porous tubular graphitic carbon nitride (g-C <sub>3</sub> N <sub>4</sub> ) on carbon cloth (CC).	Photodegradation of ciprofloxacin under visible light irradiation.	<ul style="list-style-type: none"> <li>98% of ciprofloxacin was removed within 60 min.</li> <li>CQDs improved light absorption and reduced the rapid recombination of photogenerated carriers.</li> </ul>	[18]
Carbon quantum dots (CQDs) from Arabian dates coupled with graphitic carbon nitride (AD-CQDs/ g-C <sub>3</sub> N <sub>4</sub> )	Photodegradation of 2,4-dichlorophenol (4-DCP) under sunlight irradiation.	<ul style="list-style-type: none"> <li>AD-CQDs (20 wt.%) degraded 100% of 2,4-DCP in 90 min, which was 1.7 times higher than g-C<sub>3</sub>N<sub>4</sub> (59.48%).</li> <li>CQDs increased the separation of photogenerated e<sup>-</sup>/h<sup>+</sup> and increased sensitivity towards visible light.</li> </ul>	[19]
Carbon quantum dots-modified reduced ultrathin g-C <sub>3</sub> N <sub>4</sub> (RUCN/CQD)	Photodegradation of diclofenac (DCF) under visible light irradiation.	<ul style="list-style-type: none"> <li>100% removal rate of DCF within 6 min.</li> <li>CQD enhanced the electron transfer capacity for the promoted formation of O<sub>2</sub><sup>-</sup>.</li> </ul>	[20]
Carbon quantum dots loaded with mesoporous g-C <sub>3</sub> N <sub>4</sub> (mpg-C <sub>3</sub> N <sub>4</sub> /CQDs)	Photodegradation of fluoroquinolone antibiotics under visible light irradiation.	<ul style="list-style-type: none"> <li>The removal of fluoroquinolone antibiotics was 90.1% in the presence of mpg-C<sub>3</sub>N<sub>4</sub> /CQDs, whereas it was only 65.6% when mpg-C<sub>3</sub>N<sub>4</sub> was used.</li> <li>The up-converted PL properties and efficient charge separation capacities of the CQDs enhanced the removal reaction.</li> </ul>	[21]
g-C <sub>3</sub> N <sub>4</sub> /carbon dots nanosheets calcined at 500 °C (C-CN-NS500)	Photodegradation of sulfadiazine (SDZ) under visible light.	<ul style="list-style-type: none"> <li>97.82% SDZ could be removed after 60 min.</li> <li>The degradation rate of SDZ was around 2.4 times larger than that of g-C<sub>3</sub>N<sub>4</sub>/carbon dots (C-CN).</li> <li>The effect of quantum confinement, increased specific surface area, improved separation efficiency, and prolonged contact time for the catalyst promoted the degradation of SDZ.</li> </ul>	[22]
Carbon quantum dots/CdS quantum dots/g-C <sub>3</sub> N <sub>4</sub> (CDs/CdS/GCN)	Simultaneous photocatalytic production of hydrogen coupled with degradation of bisphenol A (BPA).	<ul style="list-style-type: none"> <li>The degradation rate of BPA was 72%. The CQDs enhanced visible light absorption and have good electrical conductivity.</li> </ul>	[23]
g-C <sub>3</sub> N <sub>4</sub> modified with carbon quantum dots (CQDs)	Photodegradation of carbamazepine (CBZ) under visible light irradiation.	<ul style="list-style-type: none"> <li>CBZ degradation kinetics are more than 5 times higher.</li> <li>Surface-bonded CQDs did not alter the band gap structure of g-C<sub>3</sub>N<sub>4</sub>, but greatly inhibited the charge recombination.</li> </ul>	[24]
g-C <sub>3</sub> N <sub>4</sub> incorporated with water hyacinth leaves derived CQDs	Photodegradation of 2,4-dichlorophenol (2,4-DCP) under UV light irradiation.	<ul style="list-style-type: none"> <li>The rate constant was 0.0186–0.0194 min<sup>-1</sup>, which is 1.7 times higher than that of pure g-C<sub>3</sub>N<sub>4</sub>.</li> <li>CQDs prolonged the charge carrier lifetime, good visible light absorption, and high specific surface area.</li> </ul>	[25]

## 2. Results

### 2.1. X-ray Diffraction (XRD) and Fourier Transform Infrared Spectroscopy (FT-IR) Analyses

The XRD diffractogram of the photocatalysts is provided in Figure 1a. The single broad peak at  $2\theta = 27.1^\circ$  observed in the XRD diffractogram of the CDs corresponds to the interlayer spacing of 3.77 Å. This value is found to be larger than the distance between the (002) planes in bulk graphite (3.34 Å). Hence, it is concluded that CDs may have a turbostratic carbon structure [26]. Carbonaceous materials in this class have an amorphous carbon phase and crystalline phase [27]. The strong diffraction peak at  $2\theta = 27.4^\circ$  and weak peak at  $2\theta = 12.9^\circ$  observed in the diffractogram of pristine g-C<sub>3</sub>N<sub>4</sub> corresponds to its (002) and (100) diffraction planes. These planes are attributed to the structure of the tri-s-triazine unit with interplanar spacing and the conjugated aromatic system, respectively [28]. The XRD peaks related to CQDs were not observed in the nanocomposites due to the low carbon content and its relatively low diffraction intensity in the composites [29]. The g-C<sub>3</sub>N<sub>4</sub> peak at  $2\theta = 12.9^\circ$  lost its intensity, whereas the peak at  $2\theta = 27.4^\circ$  broadened after the incorporation of CDs. The changes indicate that the incorporation of CDs has resulted in g-C<sub>3</sub>N<sub>4</sub> crystal lattice distortion. The distortion may cause the formation of defects in g-C<sub>3</sub>N<sub>4</sub> [30]. The broadening diffraction peaks further indicate that the particle size of CDs/g-C<sub>3</sub>N<sub>4</sub> photocatalysts become smaller and thinner upon the addition of CDs.

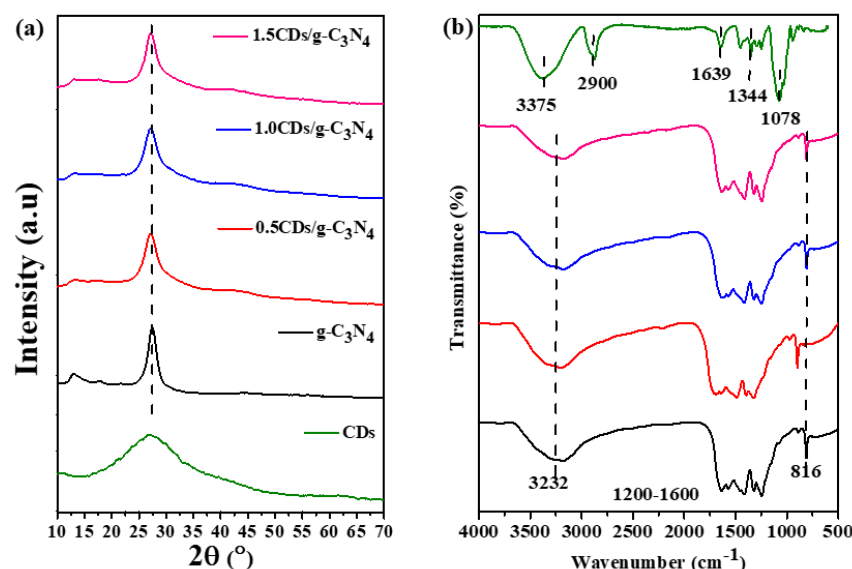


**Figure 1.** The (a) XRD diffractograms and (b) FT-IR spectra of CDs, pure g-C<sub>3</sub>N<sub>4</sub>, 0.5CDs/g-C<sub>3</sub>N<sub>4</sub>, 1.0CDs/g-C<sub>3</sub>N<sub>4</sub>, and 1.5CDs/g-C<sub>3</sub>N<sub>4</sub>.

Figure 1b illustrates the FTIR spectrum of CDs and photocatalysts. For the CDs, the peak around 3375 cm<sup>-1</sup> is related to the stretching vibration of the O–H and N–H bonds, whereas the band around 2900 cm<sup>-1</sup> is caused by the stretching vibrations of the C–H bond [31]. The band at 1639 cm<sup>-1</sup> is assigned to the stretching vibrations of C–O and the bending vibrations of N–H [32]. The band at 1344 cm<sup>-1</sup> is related to the stretching vibration of the C–N and N–H bonds [31]. The IR band at 1078 cm<sup>-1</sup> is assigned to the C–N stretching [33].

For pure g-C<sub>3</sub>N<sub>4</sub>, the sharp absorption band at 816 cm<sup>-1</sup> is assigned to the bending mode of triazine units. The several absorption bands in the region 1200–1600 cm<sup>-1</sup> are due to the stretching vibration of the CN heterocycle. This is evidence of the successful synthesis of g-C<sub>3</sub>N<sub>4</sub>. The broad peak at 3232 cm<sup>-1</sup> is assigned to the –NH and –OH stretching due to the free amino group and adsorbed water molecules [34].

The FT-IR spectra of CDs/g-C<sub>3</sub>N<sub>4</sub> photocatalysts were identical to the spectrum of pure g-C<sub>3</sub>N<sub>4</sub>. Significant changes were not observed in the photocatalysts' spectra due to the low concentration of CDs. As a consequence of the reduced loading of the CDs', the

related CN heterocycles and triazine units of the  $g\text{-C}_3\text{N}_4$  absorption bands were preserved for all CDs/ $g\text{-C}_3\text{N}_4$  photocatalysts [25]. The decrease in the intensity of the peaks provide strong support of the successful modification of  $g\text{-C}_3\text{N}_4$  by CDs [35].

## 2.2. Morphological Study

Figure 2a–d illustrates the SEM images of CDs/ $g\text{-C}_3\text{N}_4$  photocatalysts. All of the photocatalysts have similar morphology as pure  $g\text{-C}_3\text{N}_4$ . Observable pores could be formed when water and  $\text{NH}_3$  escaped as gas during the polymerization process [36]. The porous and heterogeneous surface of the photocatalysts offers a better site for the adsorption of pollutants.

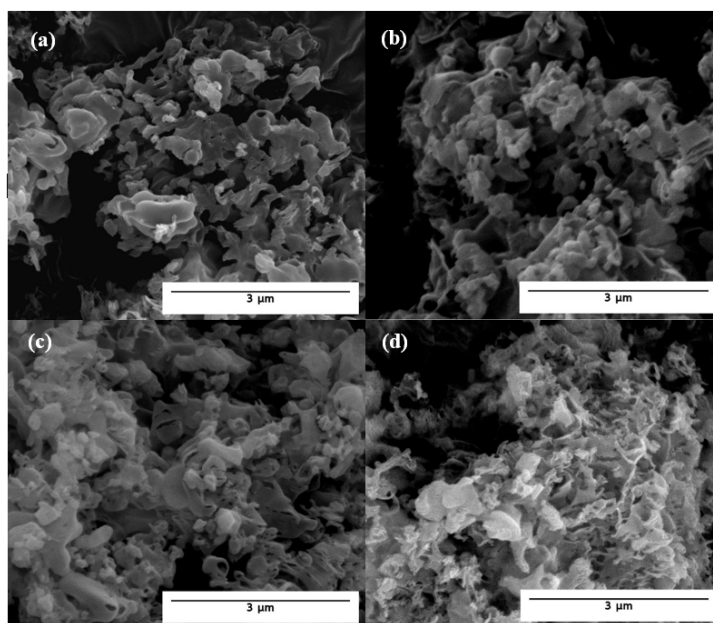


**Figure 2.** The SEM images of (a) pure  $g\text{-C}_3\text{N}_4$ , (b) 0.5CDs/ $g\text{-C}_3\text{N}_4$ , (c) 1.0CDs/ $g\text{-C}_3\text{N}_4$ , and (d) 1.5CDs/ $g\text{-C}_3\text{N}_4$ . (Magnification: 30,000 $\times$ ).

High-resolution TEM (HRTEM) analyses were used to characterize the microstructure of the photocatalysts. The HR-TEM image of the CDs (Figure 3a) revealed mono-disperse, spherical CDs with a uniform distribution. The CDs have a narrow distribution ranging from 2.2 to 3.9 nm and an average particle size of 3.75 nm, as demonstrated in Figure 3b. The absence of detectable lattice structures in the corresponding HR-TEM image indicated that the resultant CDs are amorphous. The temperature used in the synthesis of the CDs was not sufficiently high to form a fully graphitized nanostructure, which led to the formation of graphitic clusters surrounded by amorphous carbon sites. The CDs may be multi-crystalline or amorphous carbon that still contain significant  $sp^2$  clusters [37]. The distribution of CDs (small dark spots) within the matrix of  $g\text{-C}_3\text{N}_4$  can be observed in the HR-TEM images of CDs/ $g\text{-C}_3\text{N}_4$  (Figure 4d–f)).

## 2.3. Nitrogen Adsorption-Desorption Analysis

The  $\text{N}_2$  adsorption-desorption isotherms are illustrated in Figure 4. The pure  $g\text{-C}_3\text{N}_4$  and the CDs/ $g\text{-C}_3\text{N}_4$  photocatalysts exhibit the type IV isotherm, which reflect the presence of mesopores. The H3 hysteresis loop is caused by the presence of non-rigid aggregated of plate-like particles [38]. For catalytic reactions, such a mesoporous structure is advantageous because it can provide efficient pathways for the transport of reactants and products. As demonstrated in Table 2, the BET surface area of the synthesized CDs/ $g\text{-C}_3\text{N}_4$  photocatalysts was lower, compared to  $g\text{-C}_3\text{N}_4$ . The larger surface area of  $g\text{-C}_3\text{N}_4$  is ascribed to the liberation of ammonia gas in the form of bubbles during the polymerization process [39].

Similar trends were observed relative to the pore volume. Previous work provides support that the existence of CDs during the thermal polymerization of urea contributes to a substantial decline in the surface area due to a bridging effect between  $g\text{-C}_3\text{N}_4$  layers via CQDs [20]. Even though the BET surface area was reduced after the incorporation of CDs, the DFT pore size distribution (cf. Figure S1; Supplementary Materials) of the photocatalysts did not indicate significant changes. The pore sizes were mainly clustered between 2–13 nm.

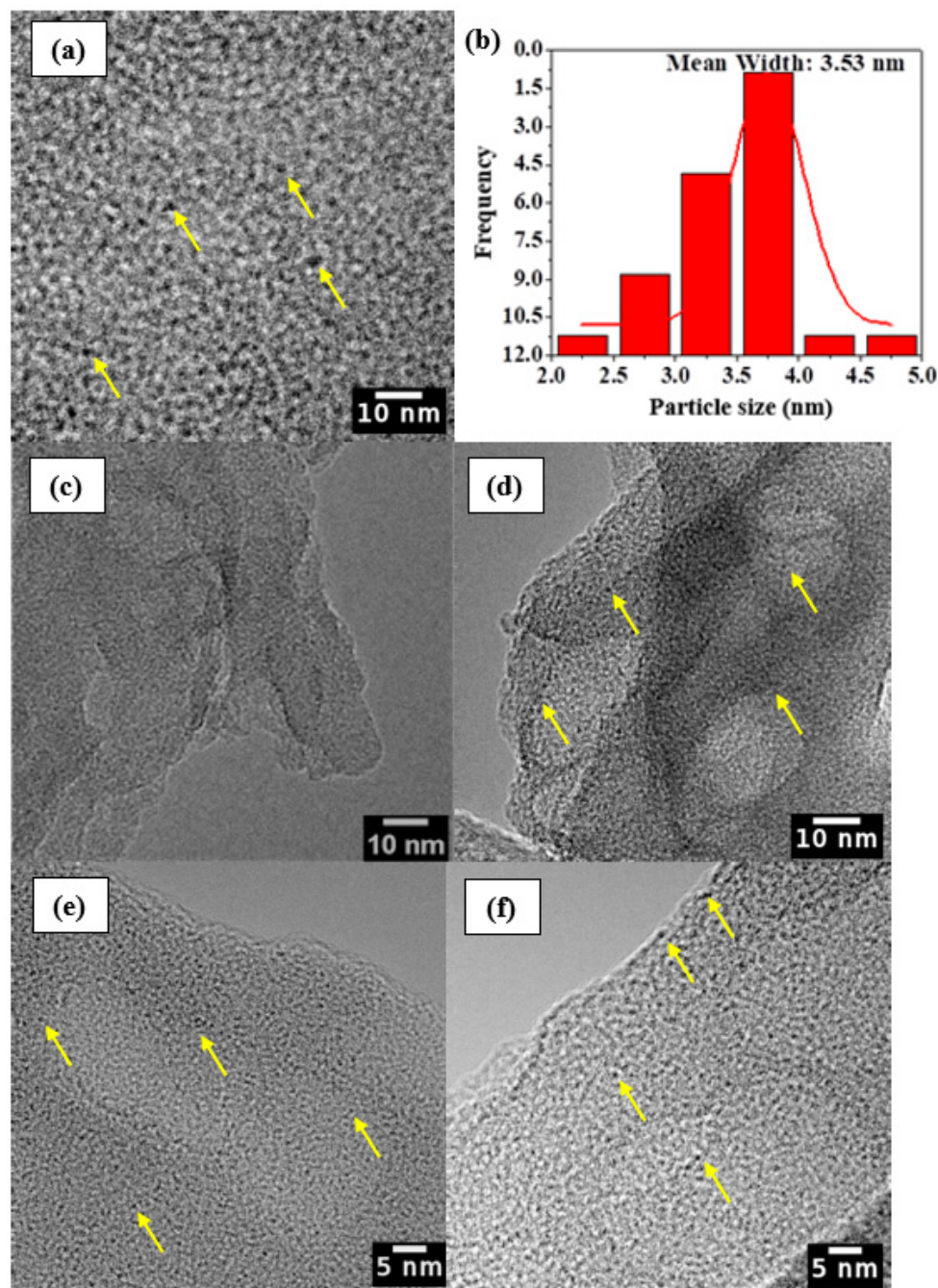


**Figure 3.** The HR-TEM images and particle size histograms of (a,b) CDs, (c) pure  $g\text{-C}_3\text{N}_4$ , (d) 0.5CDs/ $g\text{-C}_3\text{N}_4$ , (e) 1.0CDs/ $g\text{-C}_3\text{N}_4$ , and (f) 1.5CDs/ $g\text{-C}_3\text{N}_4$ . CDs are identified by yellow arrows.

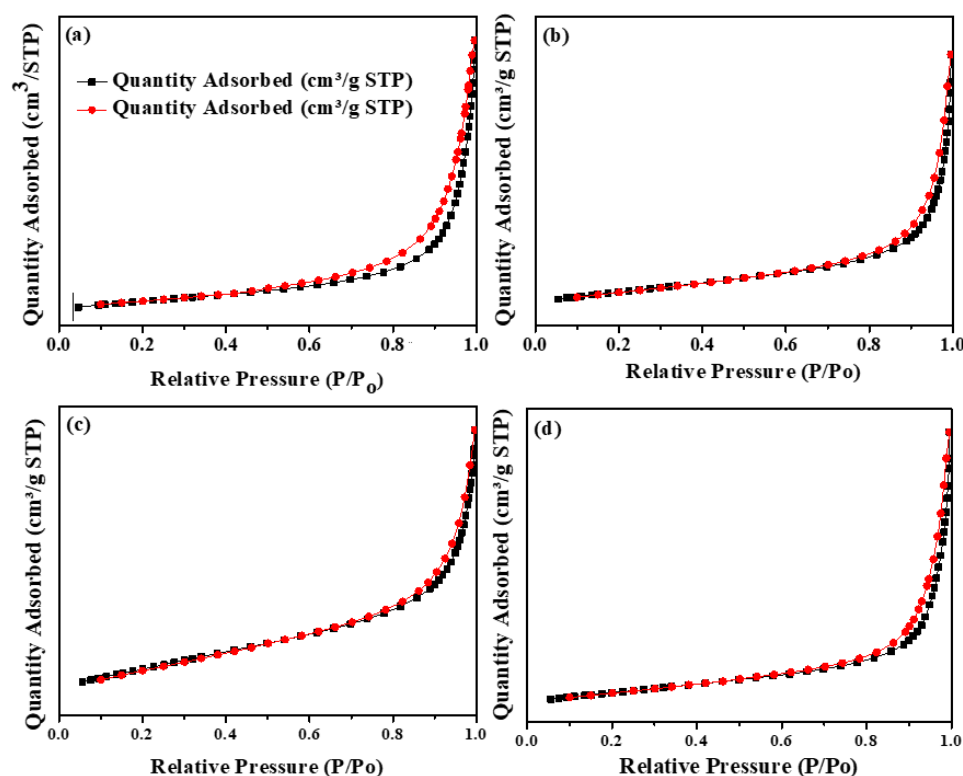


**Figure 4.** The  $N_2$  adsorption-desorption isotherms of (a) pure  $g-C_3N_4$ , (b)  $0.5CDs/g-C_3N_4$ , (c)  $1.0CDs/g-C_3N_4$ , and (d)  $1.5CDs/g-C_3N_4$ .

**Table 2.** Textural properties of the synthesized pure  $g-C_3N_4$  and  $CDs/g-C_3N_4$  photocatalysts obtained from the  $N_2$  adsorption-desorption analysis.

Samples	BET ( $m^2 g^{-1}$ )	Pore Volume ( $cm^3 g^{-1}$ )
Pure $g-C_3N_4$	62.8	0.14
$0.5CDs/g-C_3N_4$	38.5	0.06
$1.0CDs/g-C_3N_4$	48.2	0.07
$1.5CDs/g-C_3N_4$	50.08	0.09

#### 2.4. UV-Vis Absorption Analysis

The absorption spectrum of the CDs solution is illustrated in Figure 5a. The colour of the CDs solution under daylight conditions is brown, whereas irradiation under 365 nm ultraviolet (UV) light of the CDs solution yields a bright blue fluorescence emission (cf. Figure 5a inset). A shoulder observed in the range 200–250 nm is attributed to the  $\pi \rightarrow \pi^*$  transformation of aromatic  $sp^2$  domains, whereas the absorption band in the range of 250–320 nm is usually associated with the  $n \rightarrow \pi^*$  transition of a carbonyl group [40,41]. Figure 5b illustrates a plot of integrated fluorescence intensity against the corresponding absorbance for quinine sulphate (QS) and the synthesized CDs. The quantum yield (QY) of CDs in aqueous solution at an excitation wavelength of 330 nm was determined to be around 12%, using QS as a reference compares well with graphene quantum dots [42].

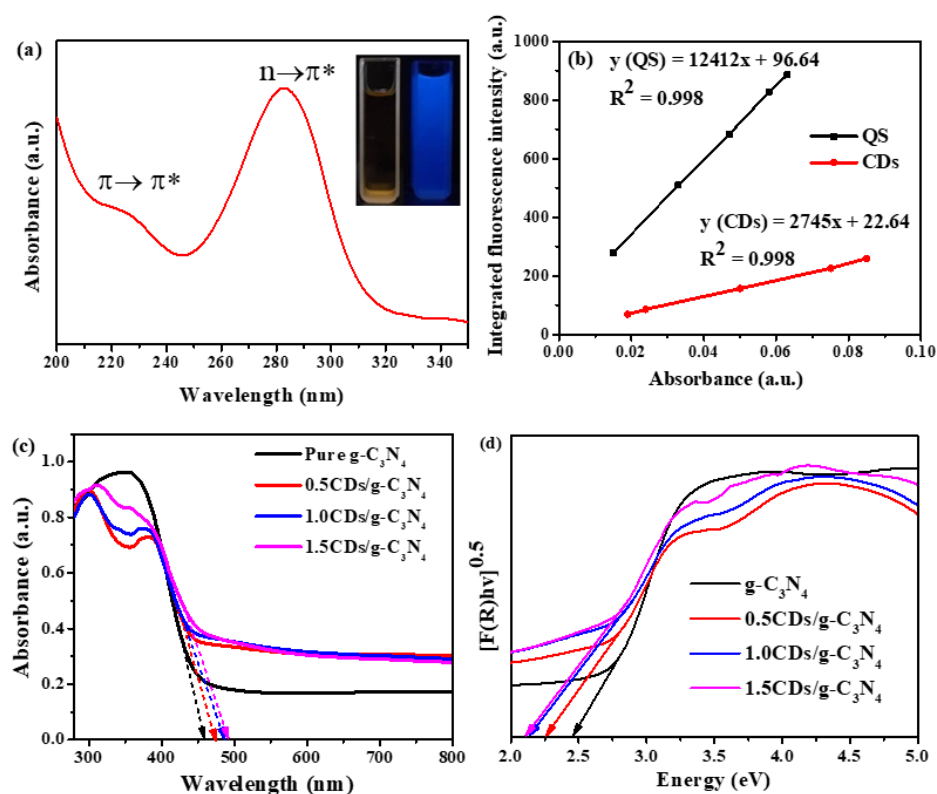


**Figure 5.** The (a) UV-Vis absorption spectrum of the CDs solution. The inset illustrates the fluorescence of the CDs solution under daylight (left) and UV Light (right), (b) plot of integrated fluorescence intensity versus the corresponding absorbance for QS and CDs, (c) UV-vis absorption spectra and (d) the Kubelka-Munk plot of the of the CDs/g-C<sub>3</sub>N<sub>4</sub> photocatalysts.

The UV-Vis absorption spectra of the CDs/g-C<sub>3</sub>N<sub>4</sub> photocatalysts are illustrated in Figure 5c. The pure g-C<sub>3</sub>N<sub>4</sub> and the CDs/g-C<sub>3</sub>N<sub>4</sub> photocatalysts displayed an absorption edge at around 459, 473, 486, and 490 nm, respectively. The bandgap energy of pure g-C<sub>3</sub>N<sub>4</sub> and CDs/g-C<sub>3</sub>N<sub>4</sub> photocatalysts were measured from optical absorption, and the corresponding plots are provided in Figure 5d. The Kubelka-Munk plot was used to evaluate the photocatalyst bandgap, where  $(F(R) \cdot hv)^{1/2}$  was plotted against photon energy (hv). Drawing a tangent line of each curve, the band gap of each photocatalyst was obtained from the x-intercept. The ability of the synthesized photocatalysts to harvest light follows the relative order: 1.5CDs/g-C<sub>3</sub>N<sub>4</sub> (2.11 eV) > 1.0CDs/g-C<sub>3</sub>N<sub>4</sub> (2.14 eV) > 0.5CDs/g-C<sub>3</sub>N<sub>4</sub> (2.26 eV) > g-C<sub>3</sub>N<sub>4</sub> (2.46 eV). The changes in band edge absorption and energy after the addition of the CDs demonstrates that CDs play an essential sensitization role in the broadening effects of the visible light absorption spectrum.

### 2.5. Photoluminescence (PL) Analysis

PL analysis was carried out to investigate the transfer and separation of the charge carriers. The PL spectra of the photocatalysts excited at 325 nm are provided in Figure 6a. The emission intensities of CDs/g-C<sub>3</sub>N<sub>4</sub> are much lower compared to that of pure g-C<sub>3</sub>N<sub>4</sub>, suggesting that a strong separation of e<sup>-</sup>/h<sup>+</sup> pairs is achieved by integrating CDs into the g-C<sub>3</sub>N<sub>4</sub> matrix. In general, a weaker PL spectrum emission intensity demonstrates a higher photoinduced carriers' separation efficiency, implying a low recombination rate [43]. The PL intensity of the CDs/g-C<sub>3</sub>N<sub>4</sub> photocatalysts was significantly lower than for pristine g-C<sub>3</sub>N<sub>4</sub>, indicating a strong suppression of the recombination of C at the heterojunction. The 1.5CDs/g-C<sub>3</sub>N<sub>4</sub> had the lowest emission intensity, suggesting that an increased amount of CDs doped into g-C<sub>3</sub>N<sub>4</sub> could greatly increase the separation efficiency of photogenerated carriers.

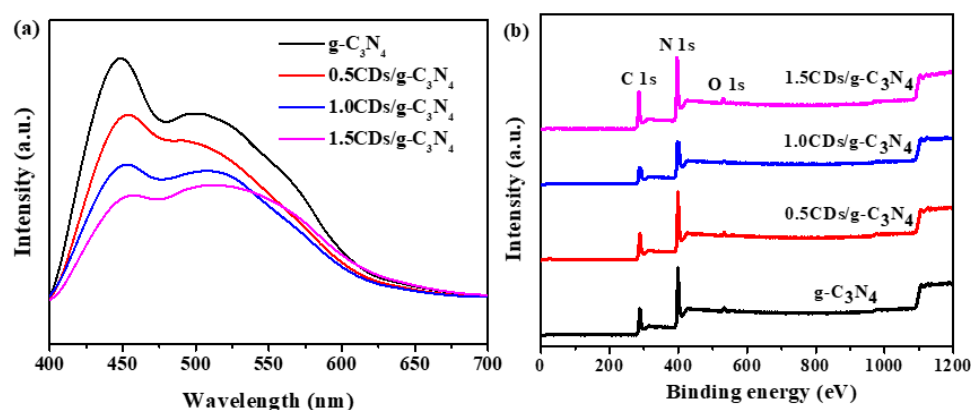


**Figure 6.** The (a) PL spectrum and (b) XPS survey spectrum of CDs/g-C<sub>3</sub>N<sub>4</sub> photocatalysts.

### 2.6. X-ray Photoelectron Spectroscopy (XPS) Analysis

The XPS survey spectrum in Figure 6b depicts the presence of carbon (C 1s), nitrogen (N 1s), and oxygen (O 1s) elements in the g-C<sub>3</sub>N<sub>4</sub> and CDs/g-C<sub>3</sub>N<sub>4</sub> nanocomposites. The deconvolution of the peaks was carried out only for g-C<sub>3</sub>N<sub>4</sub> and 1.5CDs/g-C<sub>3</sub>N<sub>4</sub> since no significant changes were noted in the survey spectra.

For pure g-C<sub>3</sub>N<sub>4</sub>, the high-resolution C 1s spectrum in (cf. Figure S2a; Supplementary Materials) demonstrated three bands at several binding energies of 284.6, 286.8, and 287.8 eV, reflecting graphitic carbon C-[C,H], adventitious carbon [44], the existence of C-NH [45], and C-(N)<sub>3</sub> group [46], respectively. The deconvoluted peaks of C 1s of 1.5CDs/g-C<sub>3</sub>N<sub>4</sub> into four peaks at 281.5, 284.6, 285.5, and 287.5 eV correspond to the graphitic carbon or *sp*<sup>2</sup> (N-C=N) [47], adventitious carbon (C-C), defect-containing *sp*<sup>2</sup>-hybridized carbons [48], and formation of C-O [49], respectively.

Three different peaks appeared in the N 1s spectra of pure g-C<sub>3</sub>N<sub>4</sub> at 396.6, 398.1, and 400.1 eV in cf. Figure S2b (Supplementary Materials). These bands are attributed to C-N [50], *sp*<sup>2</sup> hybrid N bond (C-N=C) [51], and tertiary N-(C)<sub>3</sub> [52]. For the N 1s spectrum for 1.5CDs/g-C<sub>3</sub>N<sub>4</sub>, it was deconvoluted into three bands at 395.0, 395.8, and 397.4 eV. The peak at 395.0 eV corresponds to C-N bond in amorphous carbon nitride [53], 395.8 eV is assigned to C-N=C bonding [54], and 397.4 eV also corresponds to *sp*<sup>2</sup> hybridization of nitrogen (C-N-C) [55]. As demonstrated in Figure S2c (Supplementary Materials), with regard to the O 1s spectra of pure g-C<sub>3</sub>N<sub>4</sub>, the peaks at 530.9 and 531.9 eV relate to the O-H signature for absorbed water [56]. The O 1s spectrum of 1.5CDs/g-C<sub>3</sub>N<sub>4</sub> was deconvoluted into two peaks. The binding energy 529.2 eV is assigned to C-O bonding while 532.3 eV may result due to the composition of the absorbed water or carbon dioxide and the oxygenated intermediates that did not fully react [57].

### 2.7. Photocatalytic Performance

The photocatalytic performance of pure g-C<sub>3</sub>N<sub>4</sub> and CDs/g-C<sub>3</sub>N<sub>4</sub> systems were evaluated for the photodegradation of bisphenol A (BPA) under visible light irradiation ( $\lambda > 400$  nm). The BPA removal efficiency (%) was calculated using Equation (1):

$$\% \text{ Removal efficiency} = \frac{(C_0 - C_t)}{C_0} \times 100 \quad (1)$$

where  $C_0$  and  $C_t$  are the initial and final concentrations of BPA in the solution, respectively. Kinetics contributes to a greater understanding of pollutant degradation processes, where it was reported that the photocatalytic degradation of a pollutant follows the pseudo-first-order kinetic model [58], according to the following expression:

$$-\ln \frac{C_t}{C_0} = kt \quad (2)$$

The effect of initial pH on the BPA photodegradation was studied at an initial pH of 3, 5, 7, 9, 10, and 11 using 1.5CDs/g-C<sub>3</sub>N<sub>4</sub>. The concentration of BPA and dosage of photocatalyst was fixed at 10 mg L<sup>-1</sup> and 30 mg L<sup>-1</sup>, respectively. The effect of initial pH on BPA removal is illustrated in Figure S3a (cf. Supplementary Materials). The adsorption of BPA under dark conditions for 30 min was 86%, 90%, 87%, 71%, 41%, and 4% at pH 3, 5, 7, 9, 10, and 11, respectively. The pHP<sub>ZC</sub> of the photocatalyst was 5.47, according to the pH drift method. Above the pHP<sub>ZC</sub>, the surface of the photocatalyst will be negatively charged. The molecular form of BPA exists as an anion (pK<sub>a1</sub> = 9.59) or dianion (pK<sub>a2</sub> = 11.30) under acid or alkaline conditions. The BPA molecule dissociates in aqueous media as a mono BPA<sup>-</sup> or divalent BPA<sup>2-</sup> anions within its pK<sub>a1</sub> and pK<sub>a2</sub> range. As the pH became more alkaline (pH 9–11), the highly negative photocatalyst surface will repel the negatively charged divalent BPA<sup>2-</sup> anions, leading to lower adsorption. Since the surface of 1.5CDs/g-C<sub>3</sub>N<sub>4</sub> is not saturated with BPA, irradiated light can reach its surface for the generation of e<sup>-</sup>/h<sup>+</sup> pairs, which generates ROS for the photodegradation process.

The adsorption of BPA on the surface of 1.5CDs/g-C<sub>3</sub>N<sub>4</sub> is reasonably high at pH 3–7. Even though electrostatic repulsion does exist at this range, the repulsion is weak compared to other interactions such as hydrogen bonding between the functional group (e.g., -NH<sub>2</sub> and -OH) on the photocatalyst's surface with BPA molecules. Hence, it is concluded the removal of BPA at pH 3 to 7 using 1.5CDs/g-C<sub>3</sub>N<sub>4</sub> was mainly due to adsorption rather than photocatalysis. At pH 9–11, the removal of BPA was mainly due to photocatalysis, where the highest BPA removal (49%) was achieved at pH 10. As demonstrated in Figure S3b in the Supplementary Materials, the photocatalytic reaction follows a pseudo-first-order kinetic profile. The calculated *k* values for pH 9, 10, and 11 were 0.00548, 0.0097, and 0.00479 min<sup>-1</sup>, respectively, which reflects the maximum rate constant at pH 10 for BPA degradation. Hence, the consecutive investigation was carried out at pH 10. The effect of initial BPA concentration (5, 10, 20, and 30 mg L<sup>-1</sup>) on the photocatalytic activity of 1.5CDs/g-C<sub>3</sub>N<sub>4</sub> is illustrated in Figure S4a of the Supplementary Materials. At the lowest BPA concentration (5 mg L<sup>-1</sup>), the ratio of the initial number of BPA molecules to the available adsorption site is low and, subsequently, the fractional adsorption becomes independent of the initial concentration. This means that the adsorption of the BPA molecules on the adsorption site was rapid and reached equilibrium more rapidly [59,60]. As a result, the BPA removal at 5 mg L<sup>-1</sup> is driven by adsorption. Further increases in the initial BPA concentration decreased the level of adsorption (%) since all the adsorption sites were occupied. Irradiation with visible light resulted in 80–90% removal. Hence, it is concluded that at an initial BPA concentration of 10–30 mg L<sup>-1</sup>, BPA removal is driven by photocatalysis. The photodegradation of BPA at different initial concentrations also follows the pseudo-first-order kinetics (Figure S4b; Supplementary Materials). The calculated *k* values for initial concentration of BPA at 5, 10, 20, and 30 mg L<sup>-1</sup> are 0.0045, 0.0097, 0.0098, and 0.0075 min<sup>-1</sup>, respectively. Since the highest (90%) and fastest removal rate (*k* = 0.0098) of BPA was achieved at an initial concentration of 20 mg L<sup>-1</sup>, it was used for the optimization of other parameters.

The effect of 1.5CDs/g-C<sub>3</sub>N<sub>4</sub> dosage on BPA degradation was studied under the same experimental conditions (pH 10, 20 mg L<sup>-1</sup> BPA and 180 min irradiation time) within the range of 20 to 40 mg L<sup>-1</sup>. The degree of photodegradation of BPA was 87–90% when the photocatalyst dosage was 20 mg L<sup>-1</sup> and 30 mg L<sup>-1</sup>. The level of BPA removal decreased slightly to 85% at 40 mg L<sup>-1</sup>, due to a higher degree of turbidity (Figure S5a; Supplementary Materials). Turbidity of the reaction medium prevents effective light penetration and absorption, which leads to photodegradative reduction [61,62]. At a higher photocatalyst dosage, the nanocomposite tends to agglomerate, which promotes a reduction in the catalyst surface area, which can lead to a reduction in photocatalytic activity. The reaction rates were calculated to be 0.00919, 0.00986, and 0.00811 min<sup>-1</sup> for 20, 30 and 40 mg L<sup>-1</sup>, respectively, as illustrated in Figure S5b in the Supplementary Materials. The 30 mg L<sup>-1</sup> catalyst dose appeared to be optimal, yielding about 90%. To achieve

optimum test efficiency and conserve the photocatalyst, the optimum photocatalyst dosage was set at 30 mg L<sup>-1</sup>.

The effect of the CDs loading on the g-C<sub>3</sub>N<sub>4</sub> is demonstrated in Figure S6a in the Supplementary Materials. Varying the loading of CDs did not significantly affect the photodegradation of BPA (85–90%). The *k* values for 0.5CDs/g-C<sub>3</sub>N<sub>4</sub>, 1.0CDs/g-C<sub>3</sub>N<sub>4</sub>, and 1.5CDs/g-C<sub>3</sub>N<sub>4</sub> were 0.00847, 0.00755, and 0.00986 min<sup>-1</sup>, respectively (Figure S6b; Supplementary Materials). Based on these *k* values, photodegradation took place at a faster rate using 1.5CDs/g-C<sub>3</sub>N<sub>4</sub> due to its higher BET surface area, which yields more adsorption sites and the ability to generate photogenerated e<sup>-</sup>/h<sup>+</sup> pairs. Due to its excellent efficiency, 1.5CDs/g-C<sub>3</sub>N<sub>4</sub> was selected as the best photocatalyst.

The photocatalytic activity of 1.5CDs/g-C<sub>3</sub>N<sub>4</sub> was compared with the photocatalytic activities TiO<sub>2</sub> Degussa P25 (P25) and pure g-C<sub>3</sub>N<sub>4</sub>. The BPA removal efficiency catalyzed by P25, pure g-C<sub>3</sub>N<sub>4</sub>, and 1.5CDs/g-C<sub>3</sub>N<sub>4</sub> over constant BPA concentration and irradiation time are illustrated in Figure S7a in the Supplementary Materials. The P25 and pure g-C<sub>3</sub>N<sub>4</sub> were able to remove 52% and 49% of BPA. The higher removal (%) of 1.5CDs/g-C<sub>3</sub>N<sub>4</sub> over P25 and pure g-C<sub>3</sub>N<sub>4</sub> confirms its superior photocatalytic potential. Compared to P25 and pure g-C<sub>3</sub>N<sub>4</sub>, 1.5CDs/g-C<sub>3</sub>N<sub>4</sub> has a narrower band gap, allowing better light absorption. The porous architecture of 1.5CDs/g-C<sub>3</sub>N<sub>4</sub> increased the light-harvesting properties from bulk to the surface of the photocatalyst. These features allow the suppression of e<sup>-</sup>/h<sup>+</sup> pairs for the generation of reactive oxygen species (ROS). The kinetics of the P25 and pure g-C<sub>3</sub>N<sub>4</sub> fit pseudo-first-order kinetics, similar to 1.5CDs/g-C<sub>3</sub>N<sub>4</sub> (Figure S6b; Supplementary Materials). The measured *k* values for P25 (0.00248) and pure g-C<sub>3</sub>N<sub>4</sub> (0.00337) were lower when compared to 1.5CDs/g-C<sub>3</sub>N<sub>4</sub>.

A scavenging test was carried out to identify the ROS formed during the photodegradation reaction. Ethylenediaminetetraacetic acid (EDTA), methanol (MeOH), and ascorbic acid (AA) were added as scavengers for h<sup>+</sup>, •OH, and O<sub>2</sub><sup>•-</sup>. As displayed in Figure 7a, the photodegradation rate adopts the order: AA > MeOH > EDTA. All three scavengers affected the photodegradation rate, with a major contribution from the generated hole carriers (h<sup>+</sup>) followed by •OH and O<sub>2</sub><sup>•-</sup>.

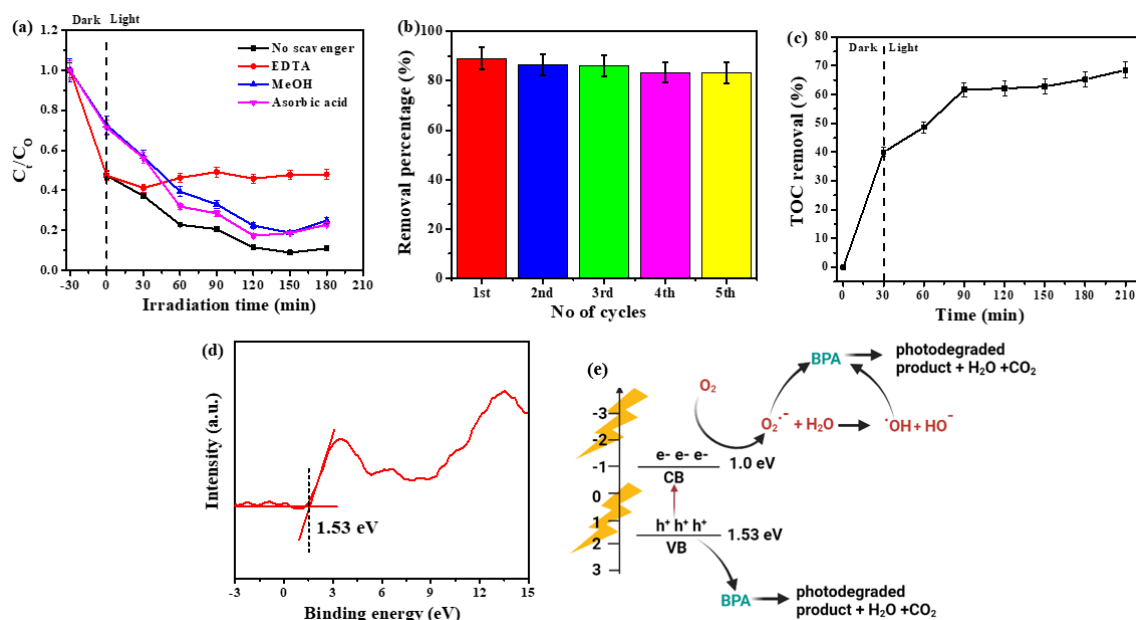


**Figure 7.** The (a) scavenging test and (b) reusability of 1.5CDs/g-C<sub>3</sub>N<sub>4</sub> carried out under visible light irradiation ([BPA] = 20 mg L<sup>-1</sup>, catalyst dosage = 30 mg L<sup>-1</sup>, pH = 10). The TOC profile is provided in (c) and (d) is the VB-XPS spectra of 1.5CDs/g-C<sub>3</sub>N<sub>4</sub>. The flow of photogenerated e<sup>-</sup>/h<sup>+</sup> is illustrated in (e).

The reusability of 1.5CDs/g-C<sub>3</sub>N<sub>4</sub> across five cycles is demonstrated in Figure 7b. At each photocatalytic experiment, over 90% of BPA was degraded by 1.5CDs/g-C<sub>3</sub>N<sub>4</sub>, which supports that the photocatalyst is highly stable. The mineralization effect of the 1.5CDs/g-C<sub>3</sub>N<sub>4</sub> nanocomposite on BPA was investigated using TOC analysis. The TOC removal demonstrated a strong mineralization pattern of BPA, as illustrated in Figure 7c. The first 30 min in the dark resulted in about 40% TOC removal through adsorption. After irradiation with light for 180 min, 67% TOC removal was achieved. The result demonstrates that 1.5CDs/g-C<sub>3</sub>N<sub>4</sub> could effectively mineralize BPA under visible light irradiation to yield CO<sub>2</sub> and H<sub>2</sub>O.

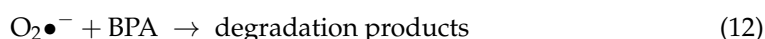
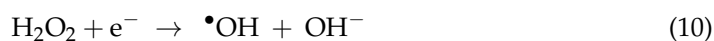
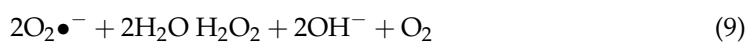
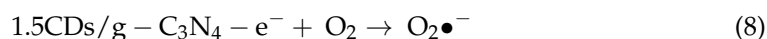
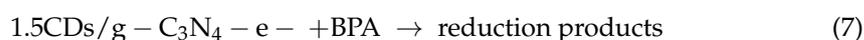
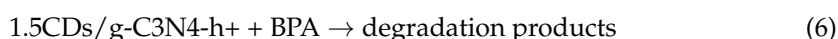
The valence band X-ray photoelectron spectroscopy (VB-XPS) was used to define the band structures of 1.5CDs/g-C<sub>3</sub>N<sub>4</sub>. The valence band (VB) and the conduction band (CB) were calculated using Equations (3) and (4).

$$E_{VB} = X - E^e + 0.5E_g \quad (3)$$

$$E_{CB} = E_{VB} - E_g \quad (4)$$

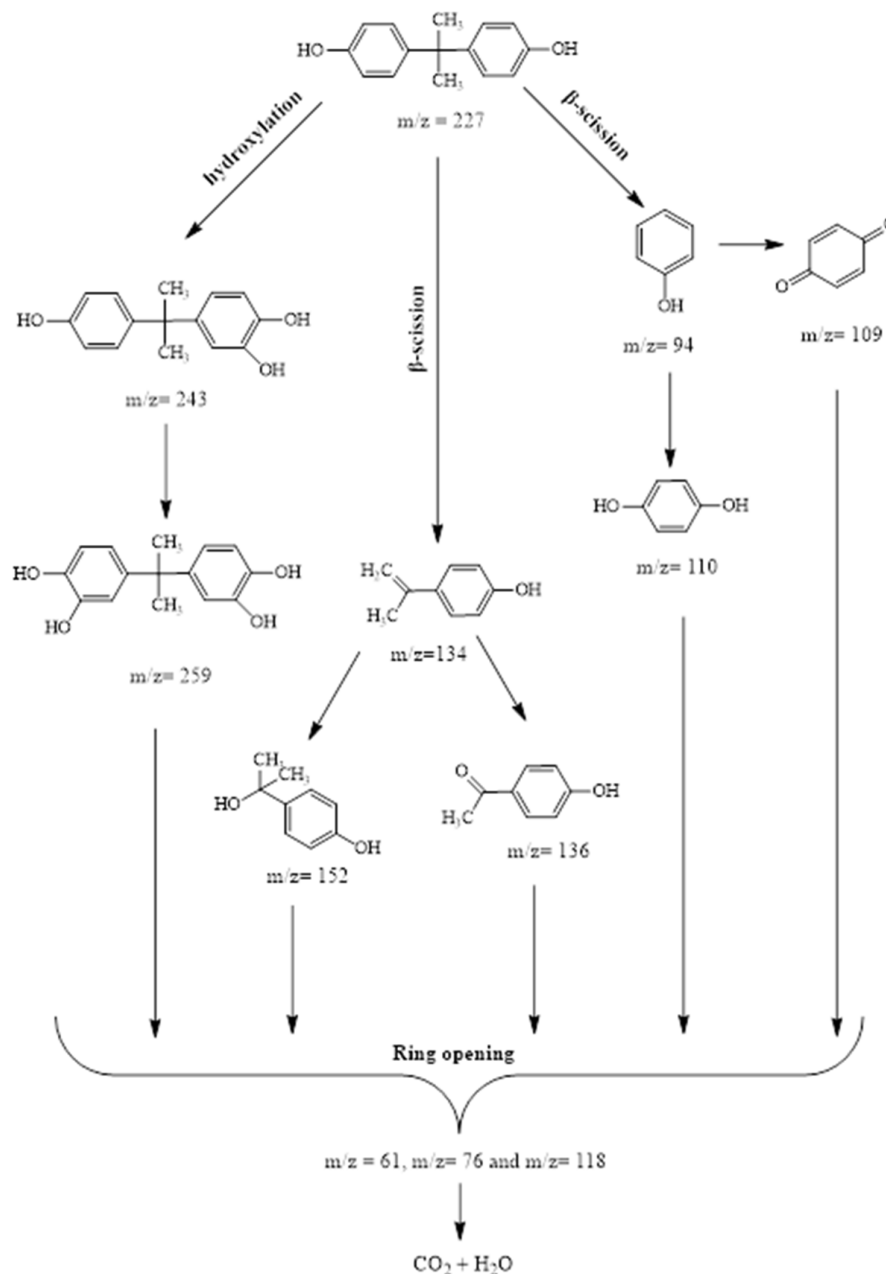
where  $E_{VB}$  is the edge potential of the VB,  $E_{CB}$  is the edge potential of the CB,  $E_g$  is the semiconductor bandgap energy,  $X$  is the semiconductor electronegativity that is the geometric mean of the constituent atoms' electronegativity and on the hydrogen scale (~4.5 eV), and  $E^e$  is the energy of free electrons. The  $E_g$  of 1.5CDs/g-C<sub>3</sub>N<sub>4</sub> is 2.11 eV.

When irradiated with light, electrons will be excited from the VB to the CB leaving behind  $h^+$  (cf. Equation (5)). The formation of the  $e^-/h^+$  pairs will trigger a series of chain reactions. As demonstrated in Figure 7d, the VB maxima of 1.5CDs/g-C<sub>3</sub>N<sub>4</sub> is 1.53 eV. The VB potential of 1.5CDs/g-C<sub>3</sub>N<sub>4</sub> is lower than  $E^0$  ( $\bullet\text{OH}/\text{OH}^-$ ) = +1.99 V vs. NHE). Hence, the photogenerated  $h^+$  are unable to oxidize  $\text{OH}^-$  into  $\bullet\text{OH}$ . However, the  $h^+$  can directly react and degrade the BPA (Equation (6)). The  $e^-$ , with photo-reducing abilities in the CB of 1.5CDs/g-C<sub>3</sub>N<sub>4</sub>, are able to convert adsorbed  $\text{O}_2$  to  $\text{O}_2^{\bullet-}$  (Equation (8)). In addition to being able to degrade BPA, the  $\text{O}_2^{\bullet-}$  is also able to form  $\bullet\text{OH}$  (Equations (9) and (10)). The  $\text{O}_2^{\bullet-}$  itself can react with BPA and mineralize it (Equation (12)). These chain reactions prevented the photogenerated  $e^-/h^+$  pairs from recombining. Hence, there is an increase in the photocatalytic activity of 1.5CDs/g-C<sub>3</sub>N<sub>4</sub>. Based on these findings, a schematic illustration indicating the transfer of photogenerated  $e^-/h^+$  pairs for the photodegradation of BPA is provided in Figure 7e.



Based on the photodegradation products identified using LC/TOF/MS, a photodegradation route is proposed, as illustrated in Scheme 1. A total of 11 aromatic intermediates were detected. At the initial stage of photodegradation, the BPA is decomposed into mono-hydroxylated BPA ( $m/z$  243), 4-isopropenylphenol ( $m/z$  134), and phenol ( $m/z$  94). The decomposition of phenol resulted in the formation of benzoquinone ( $m/z$  109) and hydroquinone ( $m/z$  110), which would eventually break down into simple organic acids. Further, hydroxylation of mono-hydroxylated BPA formed dihydroxylated BPA ( $m/z$  259) [63]. The 4-isopropenylphenol was further oxidized to easily decomposable 4-hydroxyacetophenone

( $m/z$  136) and 4-(2-hydroxyprop-2-yl)phenol [64–68]. The aromatic compounds were broken down into simple organic acids (maleic acid, glycolic acid, and acetic acid) at the end of the process, which became transformed into  $\text{CO}_2$  and  $\text{H}_2\text{O}$  via the combined oxidation of photogenerated  $\text{h}^+$ ,  $\bullet\text{OH}$ , and  $\text{O}_2^{\bullet-}$ .



**Scheme 1.** The proposed possible pathways during the photocatalytic degradation of BPA in the presence of a  $1.5\text{CDs/g-C}_3\text{N}_4$  photocatalyst.

### 3. Materials and Methods

The chemicals used were urea (>99%, QREC), glucose (>99%, QREC), titanium(IV) oxide (>99.5%, ACROS ORGANICS), bisphenol A (97%, ACROS ORGANICS), ethylenediaminetetraacetic acid (>98%, BDH Limited Poole England), ascorbic acid (>99.5%, QREC), and methanol (AR grade, QREC). All chemicals were of analytical grade and used without further purification. Ultrapure water generated by a Millipore Direct-Q™3 Ultrapure Water Purification System (ThermoFisher Scientific, Waltham, MA, USA) was used to prepare the solutions.

### 3.1. Synthesis of *g*-C<sub>3</sub>N<sub>4</sub>

The pure *g*-C<sub>3</sub>N<sub>4</sub> was synthesized using a simple thermal condensation of urea, similar to the method reported by Xu and Zhang [69]. Urea (10 g) was placed in a crucible and dried at 80 °C overnight, followed by heat treatment at 550 °C with a heating rate of 5 °C min<sup>-1</sup> for 3 h. A light-yellow powder of *g*-C<sub>3</sub>N<sub>4</sub> was obtained at the end of the heating process. The *g*-C<sub>3</sub>N<sub>4</sub> powder was ground into a fine powder and stored in a desiccator for further use.

### 3.2. Preparation of Carbon Dots (CDs)

The bottom-up method was used to synthesize the carbon dots using a one-step microwave-assisted approach. The microwave approach was chosen because its internal thermal effect creates a better distribution of heat for the CDs synthesis [70]. The carbon quantum dots (CQDs) was synthesized using glucose as a precursor. The glucose (70 mg) was dissolved in 20 mL of ultrapure water in a 150 mL beaker. The glucose solution was placed in a domestic microwave oven and heated at 500 W for 30 min. The initially transparent glucose solution changed from light to dark brown with some clustered solids. They were dissolved with 10 mL of ultrapure water to produce a light to dark brown CDs solution. The solutions were labelled as CQDs and kept in the fridge for future use.

### 3.3. Synthesis of Carbon Dots Doped Graphitic Carbon Nitride (CDs/*g*-C<sub>3</sub>N<sub>4</sub>)

The CDs/*g*-C<sub>3</sub>N<sub>4</sub> was prepared by mixing urea (10.0 g) with 40 mL of ultrapure water, followed by adding 0.5, 1.0, and 1.5 mL CDs solution. The solution was homogeneously mixed under a magnetic stirrer and heated at 80 °C until it reached complete dryness. The mixture was allowed to cool to room temperature to form a solid. The solid was ground to a powder and then calcined in a furnace at 550 °C for 2 h at a heating rate of 5 °C min<sup>-1</sup>. The photocatalysts were labelled as 0.5CDs/*g*-C<sub>3</sub>N<sub>4</sub>, 1.0CDs/*g*-C<sub>3</sub>N<sub>4</sub>, and 1.5CDs/*g*-C<sub>3</sub>N<sub>4</sub> and kept in the desiccator for further use.

### 3.4. Characterization

The prepared photocatalysts were characterized by FT-IR spectroscopy (Perkin Elmer System 2000 FT-IR Spectrophotometer) using potassium bromide (KBr) to pelletize the photocatalysts for IR analysis. The samples were analyzed in the range of 4000 to 400 cm<sup>-1</sup>. The sample crystallinity was investigated using powder X-ray diffraction (Siemens Diffractometer D5000 Kristalloflex, equipped with Cu K $\alpha$  radiation,  $\lambda = 0.154$  nm) with a step size of 0.05° from 10° to 90°. The surface morphology of the photocatalysts was investigated using SEM Leica Cambridge 360. The HRTEM analysis was carried out by HRTEM 200 kV with Field Emission, TECNAI G2 20 S-TWIN, FEI, resolution below 100 nm; it was used to determine the photocatalysts' crystallinity, particle size, and lattice fringes. The surface area of the photocatalysts was calculated using the Brunauer, Emmett, and Teller (BET) model, whilst the pore width and the pore volume was evaluated using the Density Functional Theory (DFT) method. The solid-state UV/Vis diffuse reflectance spectroscopy (UV-Visible Spectrophotometer—Cary 5000 UV NIS-NIR equipped with Lambda 35 software, Agilent Technologies, Inc., Santa Clara, CA, USA) was used to measure the band gap of the prepared photocatalysts by scanning the reflectance of the photocatalysts' from 200 to 800 nm. The photoluminescence analysis was carried out using a RAMAN-PL Spectrometer, LabRam HR, Horiba, Kyoto, Japan with  $\lambda_{\max} = 325$  nm using laser power: 30 mW equipped with a Helium-Cadmium Laser. The X-ray photoelectron spectroscopy (XPS) analysis (AXIS Ultra DLD, Kratos, equipped with an Al K $\alpha$  X-ray source—1486.6 eV at 10 mA and 15 kV to analyze a 300  $\mu\text{m} \times 700 \mu\text{m}$  area under  $7.6 \times 10^{-9}$  Torr ultra-high vacuum environment in the photocatalysts analyzing chamber) was used in measuring the elemental composition and determining the oxidation state of the photocatalysts.

### 3.5. Photocatalytic Experiments

The photodegradation of BPA ( $20 \text{ mg L}^{-1}$ ) was carried out in a 250 mL beaker with a working volume of 100 mL. The CQDs/g- $\text{C}_3\text{N}_4$  ( $50 \text{ mg L}^{-1}$ ) were loaded in BPA solution. The mixture was stirred under dark conditions for 30 min to achieve the adsorption-desorption equilibrium. The solution was then irradiated for 180 min using a 500 W xenon lamp (China) with a  $> 400 \text{ nm}$  cut-off filter glass (choot GG420 UV-filter), which was placed in between the solution and fluorescent lamp in order to prevent the UV light from reaching the nanocomposite. The intensity of the visible-light source was measured to be  $450 \text{ W m}^{-2}$ . The reactor was placed in a fume cupboard, and other regions were covered with black paper to shield the whole set-up from other light illumination sources. The reactor temperature was regulated by air supplied by an aquarium aeration pump (model BB-8000), with an air flow rate of  $20 \text{ mL min}^{-1}$ . At 30 min time intervals, 5 mL aliquots were sampled and filtered using  $0.20 \mu\text{m}$  syringe filters to remove the nanocomposite particles. The photodegradation process was monitored by analyzing the collected aliquots with a UV-Vis spectrophotometer (Schimadzu 2600 UV-Vis).

## 4. Conclusions

Carbon dots (CDs) were successfully incorporated in the matrix of g- $\text{C}_3\text{N}_4$  via the microwave-assisted thermal polymerization method. The 1.5CDs/g- $\text{C}_3\text{N}_4$  nanocomposites exhibit superior photocatalytic performance in the photodegradation of BPA under visible light irradiation, as compared with pristine g- $\text{C}_3\text{N}_4$ . The addition of CDs enhanced the light absorption capacity of the photocatalysts and suppressed the photoinduced  $e^-/h^+$  recombination rate. The removal of BPA was 90% using  $30 \text{ mg L}^{-1}$  for the photocatalyst in 100 mL of  $20 \text{ mg L}^{-1}$  BPA solution. The kinetic study demonstrated that BPA photodegradation followed a pseudo-first order rate constant. The synthesized photocatalyst retained its high degradation efficiency after five cycles, demonstrating the great potential for practical applications in environmental wastewater treatment. The LC/TOF/MS analysis identified eleven by-products, which were broken down into simple organic acids, which were further converted into  $\text{CO}_2$  and  $\text{H}_2\text{O}$  through the combined oxidation of photogenerated  $h^+$ ,  $\bullet\text{OH}$ , and  $\text{O}_2^{\bullet-}$ .

**Supplementary Materials:** The following supporting information can be downloaded at: <https://www.mdpi.com/article/10.3390/catal12111311/s1>: Figure S1. The DFT pore size distribution of (a) pure g- $\text{C}_3\text{N}_4$ , (b) 0.5CDs/g- $\text{C}_3\text{N}_4$ , (c) 1.0CDs/g- $\text{C}_3\text{N}_4$ , and (d) 1.5CDs/g- $\text{C}_3\text{N}_4$ ; Figure S2. The deconvoluted (a) C 1s, (b) N 1s, and (c) O 1s XPS spectra of 1.5CDs/g- $\text{C}_3\text{N}_4$ ; Figure S3. The (a) effect of different pH and (b) pseudo first-order kinetic fitting curves under visible light irradiation of BPA on the degradation of BPA. Reaction conditions: 1.5CDs/g- $\text{C}_3\text{N}_4$  dosage =  $30 \text{ mg L}^{-1}$ , BPA concentration =  $10 \text{ mg L}^{-1}$ , and solution volume = 100 mL; Figure S4. The (a) effect of initial concentration of BPA and (b) pseudo first-order kinetic fitting curves under visible light irradiation of BPA on the degradation of BPA. Reaction conditions: 1.5CDs/g- $\text{C}_3\text{N}_4$  dosage =  $30 \text{ mg L}^{-1}$ , solution volume = 100 mL, and pH= 10; Figure S5. The (a) effect of catalyst dosage and (b) pseudo first-order kinetic fitting curves under visible light irradiation of BPA on the degradation of BPA. Reaction conditions: BPA concentration =  $20 \text{ mg L}^{-1}$ , solution volume = 100 mL, and pH= 10; Figure S6. The (a) effect of CDs loading and (b) pseudo first-order kinetic fitting curves under visible light irradiation of BPA on the degradation of BPA. Reaction conditions: catalyst dosage =  $30 \text{ mg L}^{-1}$ , BPA concentration =  $20 \text{ mg L}^{-1}$ , solution volume = 100 mL, and pH= 10; Figure S7. The (a) effect of different photocatalysts and (b) pseudo first-order kinetic fitting curves under visible light irradiation of BPA on the degradation of BPA. Reaction conditions: catalyst amounts =  $30 \text{ mg L}^{-1}$ , BPA concentration =  $20 \text{ mg L}^{-1}$ , solution volume = 100 mL, and pH= 10.

**Author Contributions:** Conceptualization, A.I. and N.H.H.A.B.; methodology, A.I., F.B.S. and N.H.H.A.B.; validation, A.I., M.N.M.I., M.H.H. and W.H.D.; formal analysis, A.I., F.B.S., N.Y. and N.H.H.A.B.; investigation, A.I., F.B.S. and N.H.H.A.B.; resources, A.I., K.R. and N.H.H.A.B.; data curation, A.I., M.N.M.I., M.H.H., W.H.D. and N.H.H.A.B.; writing—original draft preparation, A.I., F.B.S. and N.H.H.A.B.; writing—review and editing, A.I., M.N.M.I., M.H.H., W.H.D., K.R., N.H.H.A.B. and L.D.W.; visualization, A.I., M.N.M.I. and N.H.H.A.B.; supervision, A.I., M.N.M.I. and N.H.H.A.B.; project administration, A.I.; funding acquisition, A.I., N.H.H.A.B. and L.D.W. All authors have read and agreed to the published version of the manuscript.

**Funding:** This research was funded by the Ministry of Education Malaysia (Higher Education) for the Fundamental Research Grant Scheme (FRGS/1/2019/STG01/USM/02/7).

**Acknowledgments:** Shittu Fatimah Bukola acknowledges the Federal Polytechnic Offa for the PhD sponsorship awarded to her through the Tertiary Education Trust Fund (TETFund).

**Conflicts of Interest:** The authors declare no conflict of interest.

## References

1. Colborn, T.; Clement, C. *Chemically-Induced Alterations in Sexual and Functional Development: The Wildlife/Human Connection*; Wingspread Consensus Statement; Princeton Scientific Publishing Company: Princeton, NJ, USA, 1992.
2. Zoeller, R.T.; Brown, T.R.; Doan, L.L.; Gore, A.C.; Skakkebaek, N.E.; Soto, A.M.; Woodruff, T.J.; Vom Saal, F.S. Endocrine-Disrupting Chemicals and Public Health Protection: A Statement of Principles from The Endocrine Society. *Endocrinology* **2012**, *153*, 4097–4110. [[CrossRef](#)] [[PubMed](#)]
3. Gore, A.C. Environmental Toxicant Effects on Neuroendocrine Function. *Endocrine* **2001**, *14*, 235–246. [[CrossRef](#)]
4. Carpenter, D.O. (Ed.) *Effects of Persistent and Bioactive Organic Pollutants on Human Health*; John Wiley & Sons, Inc.: Hoboken, NJ, USA, 2013. [[CrossRef](#)]
5. Yilmaz, B.; Terekci, H.; Sandal, S.; Kelestimur, F. Endocrine Disrupting Chemicals: Exposure, Effects on Human Health, Mechanism of Action, Models for Testing and Strategies for Prevention. *Rev. Endocr. Metab. Disord.* **2020**, *21*, 127–147. [[CrossRef](#)] [[PubMed](#)]
6. Welshons, W.V.; Nagel, S.C.; vom Saal, F.S. Large Effects from Small Exposures. III. Endocrine Mechanisms Mediating Effects of Bisphenol A at Levels of Human Exposure. *Endocrinology* **2006**, *147*, s56–s69. [[CrossRef](#)] [[PubMed](#)]
7. Mohapatra, D.P.; Brar, S.K.; Tyagi, R.D.; Surampalli, R.Y. Physico-Chemical Pre-Treatment and Biotransformation of Wastewater and Wastewater Sludge—Fate of Bisphenol A. *Chemosphere* **2010**, *78*, 923–941. [[CrossRef](#)]
8. Jugan, M.L.; Oziol, L.; Bimbot, M.; Huteau, V.; Tamisier-Karolak, S.; Blondeau, J.P.; Lévi, Y. In Vitro Assessment of Thyroid and Estrogenic Endocrine Disruptors in Wastewater Treatment Plants, Rivers and Drinking Water Supplies in the Greater Paris Area (France). *Sci. Total Environ.* **2009**, *407*, 3579–3587. [[CrossRef](#)]
9. Moreman, J.; Takesono, A.; Trznadel, M.; Winter, M.J.; Perry, A.; Wood, M.E.; Rogers, N.J.; Kudoh, T.; Tyler, C.R. Estrogenic Mechanisms and Cardiac Responses Following Early Life Exposure to Bisphenol A (BPA) and Its Metabolite 4-Methyl-2,4-Bis(*p*-Hydroxyphenyl)Pent-1-Ene (MBP) in Zebrafish. *Environ. Sci. Technol.* **2018**, *52*, 6656–6665. [[CrossRef](#)]
10. Wang, T.; Jiang, Z.; An, T.; Li, G.; Zhao, H.; Wong, P.K. Enhanced Visible-Light-Driven Photocatalytic Bacterial Inactivation by Ultrathin Carbon-Coated Magnetic Cobalt Ferrite Nanoparticles. *Environ. Sci. Technol.* **2018**, *52*, 4774–4784. [[CrossRef](#)]
11. Serrà, A.; Philippe, L.; Perreault, F.; Garcia-Segura, S. Photocatalytic Treatment of Natural Waters. Reality or Hype? The Case of Cyanotoxins Remediation. *Water Res.* **2021**, *188*, 116543. [[CrossRef](#)]
12. Inagaki, M.; Tsumura, T.; Kinumoto, T.; Toyoda, M. Graphitic Carbon Nitrides (g-C<sub>3</sub>N<sub>4</sub>) with Comparative Discussion to Carbon Materials. *Carbon* **2019**, *141*, 580–607. [[CrossRef](#)]
13. Liu, H.; Liang, J.; Fu, S.; Li, L.; Cui, J.; Gao, P.; Zhao, F.; Zhou, J. N Doped Carbon Quantum Dots Modified Defect-Rich g-C<sub>3</sub>N<sub>4</sub> for Enhanced Photocatalytic Combined Pollutions Degradation and Hydrogen Evolution. *Colloids Surf. A Physicochem. Eng. Asp.* **2020**, *591*, 124552. [[CrossRef](#)]
14. Cao, J.; Zhang, J.; Dong, X.; Fu, H.; Zhang, X.; Lv, X.; Li, Y.; Jiang, G. Defective Borate-Decorated Polymer Carbon Nitride: Enhanced Photocatalytic NO Removal, Synergy Effect and Reaction Pathway. *Appl. Catal. B Environ.* **2019**, *249*, 266–274. [[CrossRef](#)]
15. Wypych, G. Functional Fillers—Structure. In *Functional Fillers*; Elsevier: Amsterdam, The Netherlands, 2018; pp. 101–151. [[CrossRef](#)]
16. Sun, J.; Hui, S.; Lin, X.; Xie, J.; Wang, Q.; Li, Y.; Ying, Z. Novel g-C<sub>3</sub>N<sub>4</sub>–Carbon Dots-Aggregation/Ferrite Hybrid Heterojunction Photocatalyst with Excellent Visible-Light-Driven Photodegradation Performance toward Organic Pollutants. *Opt. Mater.* **2020**, *109*, 110242. [[CrossRef](#)]
17. Xu, Z.; Chen, Z.; Ji, T.; Jv, D.; Guan, P. The Critical Role of Surface Area Optimization in Carbon Quantum Dots Modified g-C<sub>3</sub>N<sub>4</sub> for Photocatalytic Enhancement. *Mater. Lett.* **2022**, *309*, 131273. [[CrossRef](#)]
18. Wang, Y.; Li, X.; Lei, W.; Zhu, B.; Yang, J. Novel Carbon Quantum Dot Modified g-C<sub>3</sub>N<sub>4</sub> Nanotubes on Carbon Cloth for Efficient Degradation of Ciprofloxacin. *Appl. Surf. Sci.* **2021**, *559*, 149967. [[CrossRef](#)]

19. Sim, L.C.; Tai, J.Y.; Leong, K.H.; Saravanan, P.; Tan, S.T.; Chong, W.C.; Aziz, A.A. Metal Free and Sunlight Driven g-C<sub>3</sub>N<sub>4</sub> Based Photocatalyst Using Carbon Quantum Dots from Arabian Dates: Green Strategy for Photodegradation of 2,4-Dichlorophenol and Selective Detection of Fe<sup>3+</sup>. *Diam. Relat. Mater.* **2021**, *120*, 108679. [[CrossRef](#)]
20. Liu, W.; Li, Y.; Liu, F.; Jiang, W.; Zhang, D.; Liang, J. Visible-Light-Driven Photocatalytic Degradation of Diclofenac by Carbon Quantum Dots Modified Porous g-C<sub>3</sub>N<sub>4</sub>: Mechanisms, Degradation Pathway and DFT Calculation. *Water Res.* **2019**, *151*, 8–19. [[CrossRef](#)]
21. Wang, Y.; Wang, F.; Feng, Y.; Xie, Z.; Zhang, Q.; Jin, X.; Liu, H.; Liu, Y.; Lv, W.; Liu, G. Facile Synthesis of Carbon Quantum Dots Loaded with Mesoporous g-C<sub>3</sub>N<sub>4</sub> for Synergistic Absorption and Visible Light Photodegradation of Fluoroquinolone Antibiotics. *Dalton Trans.* **2018**, *47*, 1284–1293. [[CrossRef](#)]
22. Duan, B.; Dong, C.; Yuan, X.; Yao, K. Electrospinning of Chitosan Solutions in Acetic Acid with Poly(Ethylene Oxide). *J. Biomater. Sci. Polym. Ed.* **2004**, *15*, 797–811. [[CrossRef](#)]
23. Jiang, X.-H.; Wang, L.-C.; Yu, F.; Nie, Y.-C.; Xing, Q.-J.; Liu, X.; Pei, Y.; Zou, J.-P.; Dai, W.-L. Photodegradation of Organic Pollutants Coupled with Simultaneous Photocatalytic Evolution of Hydrogen Using Quantum-Dot-Modified g-C<sub>3</sub>N<sub>4</sub> Catalysts under Visible-Light Irradiation. *ACS Sustain. Chem. Eng.* **2018**, *6*, 12695–12705. [[CrossRef](#)]
24. Zhao, C.; Liao, Z.; Liu, W.; Liu, F.; Ye, J.; Liang, J.; Li, Y. Carbon Quantum Dots Modified Tubular g-C<sub>3</sub>N<sub>4</sub> with Enhanced Photocatalytic Activity for Carbamazepine Elimination: Mechanisms, Degradation Pathway and DFT Calculation. *J. Hazard. Mater.* **2020**, *381*, 120957. [[CrossRef](#)] [[PubMed](#)]
25. Hak, C.H.; Leong, K.H.; Chin, Y.H.; Saravanan, P.; Tan, S.T.; Chong, W.C.; Sim, L.C. Water Hyacinth Derived Carbon Quantum Dots and g-C<sub>3</sub>N<sub>4</sub> Composites for Sunlight Driven Photodegradation of 2,4-Dichlorophenol. *SN Appl. Sci.* **2020**, *2*, 1030. [[CrossRef](#)]
26. Puvvada, N.; Kumar, B.N.P.; Konar, S.; Kalita, H.; Mandal, M.; Pathak, A. Synthesis of Biocompatible Multicolor Luminescent Carbon Dots for Bioimaging Applications. *Sci. Technol. Adv. Mater.* **2012**, *13*, 045008. [[CrossRef](#)] [[PubMed](#)]
27. Ruz, P.; Banerjee, S.; Pandey, M.; Sudarsan, V.; Sastry, P.U.; Kshirsagar, R.J. Structural Evolution of Turbostratic Carbon: Implications in H<sub>2</sub> Storage. *Solid State Sci.* **2016**, *62*, 105–111. [[CrossRef](#)]
28. Cao, J.; Qin, C.; Wang, Y.; Zhang, H.; Sun, G.; Zhang, Z. Solid-State Method Synthesis of SnO<sub>2</sub>-Decorated g-C<sub>3</sub>N<sub>4</sub> Nanocomposites with Enhanced Gas-Sensing Property to Ethanol. *Materials* **2017**, *10*, 604. [[CrossRef](#)]
29. Wei, Y.; Zhang, X.; Wu, X.; Tang, D.; Cai, K.; Zhang, Q. Carbon Quantum Dots/Ni-Al Layered Double Hydroxide Composite for High-Performance Supercapacitors. *RSC Adv.* **2016**, *6*, 39317–39322. [[CrossRef](#)]
30. Fang, S.; Xia, Y.; Lv, K.; Li, Q.; Sun, J.; Li, M. Effect of Carbon-Dots Modification on the Structure and Photocatalytic Activity of g-C<sub>3</sub>N<sub>4</sub>. *Appl. Catal. B Environ.* **2016**, *185*, 225–232. [[CrossRef](#)]
31. Lin, H.; Huang, J.; Ding, L. Preparation of Carbon Dots with High-Fluorescence Quantum Yield and Their Application in Dopamine Fluorescence Probe and Cellular Imaging. *J. Nanomater.* **2019**, *2019*, 5037243. [[CrossRef](#)]
32. Yang, Y.; Cui, J.; Zheng, M.; Hu, C.; Tan, S.; Xiao, Y.; Yang, Q.; Liu, Y. One-Step Synthesis of Amino-Functionalized Fluorescent Carbon Nanoparticles by Hydrothermal Carbonization of Chitosan. *Chem. Commun.* **2012**, *48*, 380–382. [[CrossRef](#)]
33. Andrade, P.F.; Nakazato, G.; Durán, N. Additive Interaction of Carbon Dots Extracted from Soluble Coffee and Biogenic Silver Nanoparticles against Bacteria. *J. Phys. Conf. Ser.* **2017**, *838*, 012028. [[CrossRef](#)]
34. Jian, X.; Liu, X.; Yang, H.M.; Li, J.G.; Song, X.L.; Dai, H.Y.; Liang, Z.H. Construction of Carbon Quantum Dots/Proton-Functionalized Graphitic Carbon Nitride Nanocomposite via Electrostatic Self-Assembly Strategy and Its Application. *Appl. Surf. Sci.* **2016**, *370*, 514–521. [[CrossRef](#)]
35. Zhang, H.; Zhao, L.; Geng, F.; Guo, L.H.; Wan, B.; Yang, Y. Carbon Dots Decorated Graphitic Carbon Nitride as an Efficient Metal-Free Photocatalyst for Phenol Degradation. *Appl. Catal. B Environ.* **2016**, *180*, 656–662. [[CrossRef](#)]
36. Li, S.; Hu, C.; Peng, Y.; Chen, Z. One-Step Scalable Synthesis of Honeycomb-like g-C<sub>3</sub>N<sub>4</sub> with Broad Sub-Bandgap Absorption for Superior Visible-Light-Driven Photocatalytic Hydrogen Evolution. *RSC Adv.* **2019**, *9*, 32674–32682. [[CrossRef](#)] [[PubMed](#)]
37. Park, Y.; Yoo, J.; Lim, B.; Kwon, W.; Rhee, S.-W. Improving the Functionality of Carbon Nanodots: Doping and Surface Functionalization. *J. Mater. Chem. A* **2016**, *4*, 11582–11603. [[CrossRef](#)]
38. Ayinla, R.T.; Dennis, J.O.; Zaid, H.M.; Sanusi, Y.K.; Usman, F.; Adebayo, L.L. A Review of Technical Advances of Recent Palm Bio-Waste Conversion to Activated Carbon for Energy Storage. *J. Clean. Prod.* **2019**, *229*, 1427–1442. [[CrossRef](#)]
39. Xu, J.; Li, Y.; Peng, S.; Lu, G.; Li, S. Eosin Y-Sensitized Graphitic Carbon Nitride Fabricated by Heating Urea for Visible Light Photocatalytic Hydrogen Evolution: The Effect of the Pyrolysis Temperature of Urea. *Phys. Chem. Chem. Phys.* **2013**, *15*, 7657. [[CrossRef](#)]
40. John, B.K.; John, N.; Mathew, S.; Korah, B.K.; Punnoose, M.S.; Mathew, B. Fluorescent Carbon Quantum Dots as a Novel Solution and Paper Strip-Based Dual Sensor for the Selective Detection of Cr(VI) Ions. *Diam. Relat. Mater.* **2022**, *126*, 109138. [[CrossRef](#)]
41. Zhang, C.; Yu, X.; Shi, X.; Han, Y.; Guo, Z.; Liu, Y. Development of Carbon Quantum Dot-Labeled Antibody Fluorescence Immunoassays for the Detection of Morphine in Hot Pot Soup Base. *Food Anal. Methods* **2020**, *13*, 1042–1049. [[CrossRef](#)]
42. Guo, Y.; Zhang, L.; Cao, F.; Leng, Y. Thermal Treatment of Hair for the Synthesis of Sustainable Carbon Quantum Dots and the Applications for Sensing Hg<sup>2+</sup>. *Sci. Rep.* **2016**, *6*, 35795. [[CrossRef](#)]
43. Li, Y.; Wu, M.; Wang, Y.; Yang, Q.; Li, X.; Zhang, B.; Yang, D. Novel P-n Li<sub>2</sub>SnO<sub>3</sub>/g-C<sub>3</sub>N<sub>4</sub> Heterojunction With Enhanced Visible Light Photocatalytic Efficiency Toward Rhodamine B Degradation. *Front. Chem.* **2020**, *8*, 75. [[CrossRef](#)]
44. Alwin, E.; Kočí, K.; Wojcieszak, R.; Zieliński, M.; Edelmánová, M.; Pietrowski, M. Influence of High Temperature Synthesis on the Structure of Graphitic Carbon Nitride and Its Hydrogen Generation Ability. *Materials* **2020**, *13*, 2756. [[CrossRef](#)] [[PubMed](#)]

45. Zhao, F.; Cheng, H.; Hu, Y.; Song, L.; Zhang, Z.; Jiang, L.; Qu, L. Functionalized Graphitic Carbon Nitride for Metal-Free, Flexible and Rewritable Nonvolatile Memory Device via Direct Laser-Writing. *Sci. Rep.* **2014**, *4*, 5882. [[CrossRef](#)] [[PubMed](#)]
46. Wang, P.; Sun, S.; Zhang, X.; Ge, X.; Lü, W. Efficient Degradation of Organic Pollutants and Hydrogen Evolution by g-C<sub>3</sub>N<sub>4</sub> Using Melamine as the Precursor and Urea as the Modifier. *RSC Adv.* **2016**, *6*, 33589–33598. [[CrossRef](#)]
47. Jin, X.; Zhong, Y.; Chen, L.; Xu, L.; Wu, Y.; Fu, F.F. A Palladium-Doped Graphitic Carbon Nitride Nanosheet with High Peroxidase-Like Activity: Preparation, Characterization, and Application in Glucose Detection. *Part. Part. Syst. Charact.* **2018**, *35*, 1700359. [[CrossRef](#)]
48. Liu, Z.; Jiang, Y.; Liu, X.; Zeng, G.; Shao, B.; Liu, Y.; Liu, Y.; Zhang, W.; Yan, M.; He, X. Silver Chromate Modified Sulfur Doped Graphitic Carbon Nitride Microrod Composites with Enhanced Visible-Light Photoactivity towards Organic Pollutants Degradation. *Compos. Part B Eng.* **2019**, *173*, 106918. [[CrossRef](#)]
49. Huang, J.; Li, D.; Li, R.; Zhang, Q.; Chen, T.; Liu, H.; Liu, Y.; Lv, W.; Liu, G. An Efficient Metal-Free Phosphorus and Oxygen Co-Doped g-C<sub>3</sub>N<sub>4</sub> Photocatalyst with Enhanced Visible Light Photocatalytic Activity for the Degradation of Fluoroquinolone Antibiotics. *Chem. Eng. J.* **2019**, *374*, 242–253. [[CrossRef](#)]
50. Ji, S.; Yang, Y.; Li, X.; Liu, H.; Zhou, Z. Facile Production of a Fenton-like Photocatalyst by Two-Step Calcination with a Broad PH Adaptability. *Nanomaterials* **2020**, *10*, 676. [[CrossRef](#)]
51. Gu, L.; Dong, G.; Yu, H.; Qiao, X.; Zhang, K.; Lu, X.; Wen, H. Graphitic Carbon Nitride-Doped Sewage Sludge as a Novel Material for Photodegradation of Eriochrome Black T. *Environ. Sci. Pollut. Res.* **2020**, *27*, 27971–27983. [[CrossRef](#)]
52. Wang, A.; Wang, C.; Fu, L.; Wong-Ng, W.; Lan, Y. Recent Advances of Graphitic Carbon Nitride-Based Structures and Applications in Catalyst, Sensing, Imaging, and LEDs. *Nano-Micro Lett.* **2017**, *9*, 47. [[CrossRef](#)]
53. Ju, H.; Yu, D.; Xu, J.; Yu, L.; Geng, Y.; Gao, T.; Yi, G.; Bian, S. Microstructure, Mechanical, and Tribological Properties of Niobium Vanadium Carbon Nitride Films. *J. Vac. Sci. Technol. A Vac. Surf. Film.* **2018**, *36*, 031511. [[CrossRef](#)]
54. Jiang, Z.; Zhang, X.; Chen, H.S.; Hu, X.; Yang, P. Formation of g-C<sub>3</sub>N<sub>4</sub> Nanotubes towards Superior Photocatalysis Performance. *ChemCatChem* **2019**, *11*, 4558–4567. [[CrossRef](#)]
55. Tang, R.; Ding, R.; Xie, X. Preparation of Oxygen-Doped Graphitic Carbon Nitride and Its Visible-Light Photocatalytic Performance on Bisphenol A Degradation. *Water Sci. Technol.* **2018**, *78*, 1023–1033. [[CrossRef](#)] [[PubMed](#)]
56. Yang, Q.; Chen, C.; Zhang, Q.; Zhang, Z.; Fang, X. Molecular Engineering of Supramolecular Precursor to Modulate g-C<sub>3</sub>N<sub>4</sub> for Boosting Photocatalytic Hydrogen Evolution. *Carbon* **2020**, *164*, 337–348. [[CrossRef](#)]
57. Yin, J.-T.; Li, Z.; Cai, Y.; Zhang, Q.-F.; Chen, W. Ultrathin Graphitic Carbon Nitride Nanosheets with Remarkable Photocatalytic Hydrogen Production under Visible LED Irradiation. *Chem. Commun.* **2017**, *53*, 9430–9433. [[CrossRef](#)] [[PubMed](#)]
58. Liu, W.; He, T.; Wang, Y.; Ning, G.; Xu, Z.; Chen, X.; Hu, X.; Wu, Y.; Zhao, Y. Synergistic Adsorption-Photocatalytic Degradation Effect and Norfloxacin Mechanism of ZnO/ZnS@BC under UV-Light Irradiation. *Sci. Rep.* **2020**, *10*, 11903. [[CrossRef](#)]
59. Abdi, J.; Vossoughi, M.; Mahmoodi, N.M.; Alemzadeh, I. Synthesis of Metal-Organic Framework Hybrid Nanocomposites Based on GO and CNT with High Adsorption Capacity for Dye Removal. *Chem. Eng. J.* **2017**, *326*, 1145–1158. [[CrossRef](#)]
60. Mahmoodi, N.M.; Hayati, B.; Arami, M.; Mazaheri, F. Single and Binary System Dye Removal from Colored Textile Wastewater by a Dendrimer as a Polymeric Nanoarchitecture: Equilibrium and Kinetics. *J. Chem. Eng. Data* **2010**, *55*, 4660–4668. [[CrossRef](#)]
61. Tzeng, J.-H.; Weng, C.-H.; Chang, C.-J.; Yen, L.-T.; de Luna, M.D.G.; Huang, J.-W.; Lin, Y.-T. N-Schorel TiO<sub>2</sub> Nanocomposite for Visible-Light Photocatalysis Deactivation Yeast Exemplified by *Candida Albicans*. *Chem. Eng. J.* **2022**, *435*, 134294. [[CrossRef](#)]
62. Huang, S.-M.; Weng, C.-H.; Tzeng, J.-H.; Huang, Y.-Z.; Anotai, J.; Yen, L.-T.; Chang, C.-J.; Lin, Y.-T. Photocatalytic Inactivation of *Klebsiella Pneumoniae* by Visible-Light-Responsive N/C-Doped and N-Tourmaline/Palladium-C-Codoped TiO<sub>2</sub>. *Chem. Eng. J.* **2020**, *379*, 122345. [[CrossRef](#)]
63. Oh, W.-D.; Lok, L.-W.; Veksha, A.; Giannis, A.; Lim, T.-T. Enhanced Photocatalytic Degradation of Bisphenol A with Ag-Decorated S-Doped g-C<sub>3</sub>N<sub>4</sub> under Solar Irradiation: Performance and Mechanistic Studies. *Chem. Eng. J.* **2018**, *333*, 739–749. [[CrossRef](#)]
64. Naya, S.; Yamauchi, J.; Okubo, T.; Tada, H. Rapid Removal and Mineralization of Bisphenol A by Heterosupramolecular Plasmonic Photocatalyst Consisting of Gold Nanoparticle-Loaded Titanium(IV) Oxide and Surfactant Admicelle. *Langmuir* **2017**, *33*, 10468–10472. [[CrossRef](#)] [[PubMed](#)]
65. Zhu, Y.; Yue, M.; Natarajan, V.; Kong, L.; Ma, L.; Zhang, Y.; Zhao, Q.; Zhan, J. Efficient Activation of Persulfate by Fe<sub>3</sub>O<sub>4</sub>@β-Cyclodextrin Nanocomposite for Removal of Bisphenol A. *RSC Adv.* **2018**, *8*, 14879–14887. [[CrossRef](#)] [[PubMed](#)]
66. Ding, Y.; Zhou, P.; Tang, H. Visible-Light Photocatalytic Degradation of Bisphenol A on NaBiO<sub>3</sub> Nanosheets in a Wide PH Range: A Synergistic Effect between Photocatalytic Oxidation and Chemical Oxidation. *Chem. Eng. J.* **2016**, *291*, 149–160. [[CrossRef](#)]
67. Sharma, J.; Mishra, I.M.; Kumar, V. Mechanistic Study of Photo-Oxidation of Bisphenol-A (BPA) with Hydrogen Peroxide (H<sub>2</sub>O<sub>2</sub>) and Sodium Persulfate (SPS). *J. Environ. Manag.* **2016**, *166*, 12–22. [[CrossRef](#)] [[PubMed](#)]
68. Poerschmann, J.; Trommler, U.; Górecki, T. Aromatic Intermediate Formation during Oxidative Degradation of Bisphenol A by Homogeneous Sub-Stoichiometric Fenton Reaction. *Chemosphere* **2010**, *79*, 975–986. [[CrossRef](#)] [[PubMed](#)]
69. Xu, C.Q.; Zhang, W.D. Facile Synthesis of Nitrogen Deficient g-C<sub>3</sub>N<sub>4</sub> by Copolymerization of Urea and Formamide for Efficient Photocatalytic Hydrogen Evolution. *Mol. Catal.* **2018**, *453*, 85–92. [[CrossRef](#)]
70. Fan, L.; Yu, Q.; Chen, J.; Khan, U.; Wang, X.; Gao, J. Achievements and Perspectives in Metal-Organic Framework-Based Materials for Photocatalytic Nitrogen Reduction. *Catalysts* **2022**, *12*, 1005. [[CrossRef](#)]